RSC Advances

PAPER

View Article Online
View Journal | View Issue



Cite this: *RSC Adv.*, 2021, **11**, 36913

# A stable Ln(III)-functionalized Cd(II)-based metal–organic framework: tunable white-light emission and fluorescent probe for monitoring bilirubin†

Xiao-Qing Wang, *[a] Xuehui Ma,[a] Doudou Feng,[a] Dan Wu[a] and Jie Yang *[b]

A novel anionic Cd(II)-based metal–organic framework, $H_2[Cd_9(DDB)_4(BPP)_4(H_2O)_{14}]\cdot 4H_2O\cdot 2DMA$ (**1**), was successfully obtained with a rigid carboxylate ligand 3,5-di(2′,4′-dicarboxylphenyl)benzoic acid ($H_5DDB$) and a flexible pyridyl ligand 1,3-bis(4-pyridyl)propane (BPP). Complex **1** contains two-dimensional (2D) honeycomb structures and one-dimensional (1D) chain structures. The adjacent 2D structures are linked by strong intermolecular hydrogen bonds to form an *ABAB* 3D supramolecular structure, where the 1D chain structures traverse the channels of the 2D structures. Due to the anionic framework, Ln(III) ions (Ln = Eu and Tb) can be encapsulated in the framework of **1** by a post-synthetic modification process to obtain Ln(III)@**1**, where 1.09Eu(III)@**1** (**1a**) and 0.658Tb(III)@**1** (**1b**) can be obtained by soaking complex **1** in a $Eu(NO_3)_3\cdot 6H_2O$ or $Tb(NO_3)_3\cdot 6H_2O$ aqueous solution for 48 h. The liquid-state emission spectra of Ln(III)@**1** can be tuned to be a white light emission by changing the Eu(III)/Tb(III) molar ratio in solution. Moreover, **1b** can be used as a "turn-off" fluorescent probe for bilirubin with a low detection limit of 0.250 μM in phosphate buffer solution (pH = 7.4), which presents excellent sensitivity, high selectivity, and reusability. Furthermore, the devised fluorescent probe in serum also exhibits the fluorescence "turn-off" process with a low detection limit of 0.279 μM, and the recovery rate of bilirubin is 99.20–101.9%. The possible mechanisms of the fluorescence "turn-off" process can be explained by resonance energy transfer, and the weak interaction between **1b** and bilirubin.

Received 2nd September 2021
Accepted 25th October 2021

DOI: 10.1039/d1ra06592k

rsc.li/rsc-advances



## 1. Introduction

Bilirubin (BR) as the main catabolite of hemoglobin is not only a natural anti-oxidant that can prevent phospholipid and linoleic acid oxidation but also an endogenous toxin that could lead to damage of the nervous system.[1–3] Bilirubin can be classified into three types, including free bilirubin, direct bilirubin and total bilirubin. Generally, the free bilirubin content is an important indicator of chronic jaundice and liver diseases. In human serum, the normal content of free bilirubin is less than 17.1 μmol $L^{-1}$. A high content of >50 μmol $L^{-1}$ indicates that the person is under jaundice conditions, which can lead to brain damage, hepatitis, and even neonatal death.[4–6] Thus, it is significant to accurately and rapidly detect bilirubin concentration in human serum.

Currently, several methods have been used to monitor the bilirubin concentration, including direct spectrophotometry,[7] diazo reaction,[8] amperometric detection,[9] fluorescence analysis[10] and so on. However, direct spectrophotometry is susceptible to interference from other proteins. The pH-dependence of diazo reaction can affect the accuracy of the bilirubin determination. Amperometric detection is usually performed with BR oxidase modified the electrode surface, but the BR oxidase is unstable that can affect the accuracy determination of bilirubin. Fluorescence analysis with excellent sensitivity, high selectivity, fast response time and simple operation has attracted numerous attentions for detecting analytes. Metal–organic frameworks (MOFs) as burgeoning fluorescence materials are active in the application of luminescent sensors,[11–19] optical material[20–22] and so on. Especially, lanthanide metal–organic frameworks (Ln-MOFs) with unique optical property of Ln(III) ions have been applied as luminescent sensors to detect many analytes, including metal ions,[23] noxious anionic ions,[24] pesticides,[25] amino acids,[26] antibiotics,[27] organic solvents,[28] nitroexplosives,[29] and so on. Generally, Ln-MOFs were obtained by self-assembly of organic ligands and Ln(III) ions, which is challenging and needs a lot of experimentation. Post-synthetic modification process can be used to prepare Ln-MOFs by encapsulating Ln(III) ions in MOFs, which have the unique

[a]*Department of Chemistry, College of Science, North University of China, Taiyuan 030051, China. E-mail: xqwang@nuc.edu.cn*

[b]*Shandong Provincial Key Laboratory of Chemical Energy Storage and Novel Cell Technology, School of Chemistry and Chemical Engineering, Liaocheng University, Liaocheng 252000, China. E-mail: yangjie_lcu@126.com*

† Electronic supplementary information (ESI) available: IR spectra, PXRD patterns, TGA curves, patterns of photochemistry, ESI table, selected bond distances and angels. CCDC 1918381 for **1**. For ESI and crystallographic data in CIF or other electronic format see DOI: 10.1039/d1ra06592k

optical property of Ln(III) ions and can be applied as luminescent sensors.

Herein, a novel anionic MOF, $H_2[Cd_9(DDB)_4(BPP)_4(H_2O)_{14}]\cdot 4H_2O\cdot 2DMA$ (**1**), was successfully synthesized with a rigid carboxylate ligand 3,5-di(2′,4′-dicarboxylphenyl)benzoic acid ($H_5DDB$) and a flexible pyridyl ligand 1,3-bis(4-pyridyl)propane (BPP), which contains 2D layer structures and 1D chain structures. The Ln(III) ions (Ln = Eu and Tb) were encapsulated in the framework of **1** by post-synthetic modification process to obtain Eu(III)@**1**, Tb(III)@**1** and the Eu(III)Tb(III)@**1** mixture. A white-light-emitting source can be obtained by tuning the molar ratio of Eu(III) and Tb(III) ions. Moreover, Tb(III)@**1** was used as luminescent sensor to detect bilirubin with high selectivity and sensitively in serum system.

## 2. Experimental section

### 2.1. Materials and methods

The ligands $H_5DDB$ and BPP were acquired from Jinan Henhua Sci. & Tec. Co. Ltd. Bilirubin was purchased from Energy Chemical. Human serum samples were purchased from AmyJet Scientific Inc. The serum samples were obtained by diluting the purchased sample 20 times with phosphate buffer solutions (PBS, pH = 7.4). The powder X-ray diffraction (PXRD) was measured on a Rigaku D/Max-2500 PC diffractometer. A FTIR-8400S spectrometer was used to recorded the IR spectra. The elemental analyses was confirmed on a Vario MACRO cube elemental analyzer. Thermogravimetric analysis (TGA) was performed on a ZCT-A analyzer at 30–750 °C under $N_2$ environment. UV-vis absorption spectra was obtained from Shimadzu UV-2600 spectrophotometer. The luminescence spectra were recorded on a Hitachi F-4600 fluorescence spectrophotometer. X-ray photoelectron spectroscopy (XPS) measurements were conducted with a Thermo ESCALAB 250Xi.

### 2.2. Synthesis of $H_2[Cd_9(DDB)_4(BPP)_4(H_2O)_{14}]\cdot 4H_2O\cdot 2DMA$ (1)

A mixture of $CdCl_2\cdot 2.5H_2O$ (3.7 mg, 0.016 mmol), $H_5DDB$ (3.6 mg, 0.008 mmol) and BPP (1.6 mg, 0.008 mmol) in DMA/$H_2O$ (4.0 mL, v/v = 1/2) was sealed in a 25 mL Teflon reactor, heated to 120 °C for 55 h, and then cooled to room temperature at a rate of 3 °C $h^{-1}$. Colorless block crystals were obtained by washed with EtOH, filtration and dried in air. Calcd for $H_2[Cd_9(DDB)_4(BPP)_4(H_2O)_{14}]\cdot 4H_2O\cdot 2DMA$: C, 42.92; H, 3.40; N, 2.88. Found: C, 42.86; H, 3.35; N, 2.89. IR (KBr $cm^{-1}$): 536(w), 559(m), 595(w), 651(w), 707(w), 769(m), 858(w), 918(w), 1417(s), 1479(s), 1500(m), 1517(m), 1568(w), 1606(w), 2482(w), 2790(w).

### 2.3. Synthesis of Tb(III)@1 and Eu(III)@1

10 mg of complex **1** was uniformly dispersed in a $Eu(NO_3)_3\cdot 6H_2O$ aqueous solution (4 mL, 10 mM) and placed in a dark environment for 2 h, 4 h, 8 h, 12 h, 24 h, 48 h. Then, the mixture was washed several times with water and EtOH, filtered, dried and the Eu(III)@**1** was collected. Complex **1** soaked for 48 h was named as 1.09Eu(III)@**1** (**1a**).

Similarly, complex **1** was immersed in $Tb(NO_3)_3\cdot 6H_2O$ for 2 h, 4 h, 8 h, 12 h, 24 h and 48 h. The preparation method of Tb(III)@**1** is the same as Eu(III)@**1**, except that $Eu(NO_3)_3\cdot 6H_2O$ is replaced with $Tb(NO_3)_3\cdot 6H_2O$. Complex **1** soaked in $Tb(NO_3)_3\cdot 6H_2O$ solution for 48 h was named as 0.658Tb(III)@**1** (**1b**).

The relative molar ratios of Eu(III), Tb(III), and Cd(III) in the MOFs were calculated by inductively coupled plasma (ICP).

## 3. Results and discussion

### 3.1. Crystal structure of complex 1

The crystallographic data exhibit that **1** possesses an anionic framework, which belongs to orthorhombic crystal system with space group *Pbcm* (Table 1). Its asymmetric unit contains two individual units, naming part A and part B. Part A includes half of a Cd1(II) ion, half of a Cd2(II) ion, one Cd3(II) ion, one $DDB^{5-}$ ligand, half of a BPP ligand and two and a half of coordinated water molecules, where $H_5DDBA$ ligand is completely deprotonized and exhibits a coordination mode: $\mu_5$–$\eta^2$:$\eta^2$:$\eta^2$:$\eta^2$:$\eta^1$. Part B includes a quarter of one Cd4(II) ion, a quarter of a BPP ligand, and one coordinated water molecule (Fig. 1). Thus, the total structure of **1** is anionic. Herein, the central Cd1, Cd2, Cd4 ions are all six-coordinated with distorted octahedron geometry. Cd1 is coordinated by four O atoms from two different $DDB^{5-}$ ligands, one O atom from a coordinated water molecule, and one N atom from a BPP ligand. Cd2 is coordinated by two O atoms from two $DDB^{5-}$ ligands, three O atoms from three coordinated water molecules, and one N atom from a BPP ligand. Cd4 is coordinated by four O atoms from four coordinated water molecules, and two N atoms from two BPP ligands. Moreover, Cd3 is seven-coordinated by six O atoms from three

Table 1 Crystal data for complex **1**

| Complex | **1** |
|---|---|
| Formula | $C_{131}H_{106}Cd_9N_6O_{54}$ |
| $M_r$ | 3639.81 |
| Crystal system | Orthorhombic |
| Space group | *Pbcm* |
| $a$ (Å) | 13.9850(12) |
| $b$ (Å) | 25.773(2) |
| $c$ (Å) | 25.773(2) |
| $\alpha$ (deg.) | 90 |
| $\beta$ deg.) | 90 |
| $\gamma$ (deg.) | 90 |
| $Z$ | 2 |
| $V$ (Å$^3$) | 9289.5(14) |
| $D_c$ (g $cm^{-3}$) | 1.301 |
| $\mu$ ($mm^{-1}$) | 1.078 |
| $F$ (000) | 3596.0 |
| No. of unique reflns | 43 686 |
| No. of obs reflns [$I > 2\sigma(I)$] | 8367 |
| Parameters | 508 |
| GOF | 1.082 |
| Final $R$ indices [$I > 2\sigma(I)$][a,b] | $R_1 = 0.1003$, w$R_2 = 0.2973$ |
| $R$ indices (all data) | $R_1 = 0.1463$, w$R_2 = 0.3231$ |
| $\rho_{max}/\rho_{min}$ (e Å$^{-3}$) | 1.55 and −3.48 |

[a] $R_1 = \sum||F_o| - |F_c||/\sum|F_o|$. [b] $wR_2 = [\sum w(F_o^2 - F_c^2)^2/\sum w(F_o^2)^2]^{0.5}$.

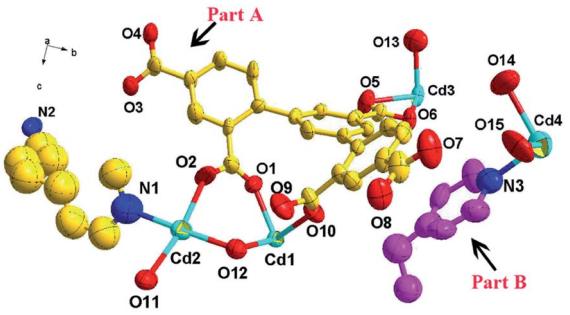


Fig. 1 The asymmetric unit of complex **1** including part A and part B.

different $DDB^{5-}$ ligands, and one O atom from coordinated $H_2O$ molecule with a $\{CdO_7\}$ geometry. The average bond distances of Cd–O and Cd–N are 2.331 Å and 2.258 Å, respectively.[30,31]

In complex **1**, a 2D honeycomb structure was formed based on the part A (Fig. 2a), and a 1D chain structure was constructed based on the part B (Fig. 2b). Due to the large windows in the 2D honeycomb structure, the 1D chain structures intersperse in the honeycomb windows (Fig. 2c). Additionally, four types of hydrogen bonds exist in complex **1** to enhance its stability (Table S2† and Fig. 2d). In the 2D structure, there are two kinds of intramolecular hydrogen bonds between the carboxylic oxygen atoms of the $DDB^{5-}$ ligand and the coordinated water molecule (O12···O9, distance 2.6489(2) Å, O12–H12A···O9, bond angle 148°; O13···O7, distance 2.9787(3), $O13^{vi}$–$H13B^{vi}$···O7, bond angle 110°). There is an intermolecular hydrogen bond between the carboxylic oxygen atoms of the $DDB^{5-}$ ligand in the 2D structure and the coordinated water molecule in the 1D structure (O15···O7, distance 2.8882(2) Å, O15–H15A···O7, bond angle 160°). Furthermore, strong intermolecular hydrogen bonds exist between the carboxylic oxygen atoms of the $DDB^{5-}$ ligand and the coordinated water molecule in the adjacent 2D structures (O13···$O5^{v}$, distance 2.7028(2) Å, O13–H13A···$O5^{v}$, bond angle 168°). The adjacent 2D structures are linked by the strong intermolecular hydrogen bonds to form an *ABAB* 3D supramolecular structure, where the 1D chain structures traverse the channels of the 2D structures (Fig. 2e). Due to the channels in the structure of **1**, the void volume was calculated to be 27.3% using PLATON.[32,33]

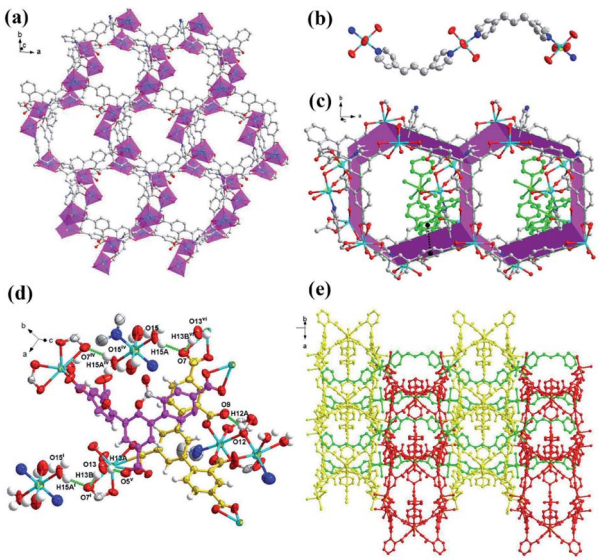


Fig. 2 (a) The 2D honeycomb structure based on part A; (b) the 1D chain structure based on part B; (c) the 1D chain structure interspersed in the windows of 2D structure (the green atoms represent 1D chain structure); (d) the intramolecular and intermolecular hydrogen bonds in complex **1**; (e) the 3D supramolecular framework for **1**. Symmetry codes: (i) $1 + x, +y, +z$; (iv) $-x, 2 - y, -z$; (v) $x, 1.5 - y, -z$; (vi) $-1 + x,y,z$.

### 3.2. Stability test

The thermostability of complex **1** was investigated under a $N_2$ atmosphere at the temperature range of 30–750 °C (Fig. S1†). From 30 °C to 100 °C, a weight loss of complex **1** is 9.12% due to the loss of four free water molecules and fourteen coordinated water molecules (calcd. 8.92%). Whereafter, a slight weight loss of 4.76% exists at the range from 100 °C to 289 °C, which corresponds to the loss of two free DMA molecules. Then with the temperature increasing, there is a sharp weight loss due to the collapse of its skeleton. In addition, the water stability and pH stability are also important for the future applications of complex **1**. Thus, the prepared **1** samples were immersed in boiling water for 48 hours and in aqueous solutions with different pH values for 24 hours. Fig. 3a shows that the PXRD of the prepared **1** sample can match with the simulation diagram, and Fig. 3b displays that their IR spectra have barely changed. The results indicate the high water stability and pH stability of complex **1**.

### 3.3. Photoluminescence properties of complex 1 and tunable luminescence

The solid-state emission spectra of **1**, $H_5DDB$ and BPP were measured at room temperature, where their fluorescence characteristic peaks are located at 463 nm ($\lambda_{ex}$ = 325 nm), 387 nm ($\lambda_{ex}$ = 317 nm), and 459 nm ($\lambda_{ex}$ = 325 nm), respectively (Fig. S2†). Compared with the luminescent spectra of $H_5DDB$ and BPP ligands, the emission peak of complex **1** presents 76 nm and 4 nm red shifts, respectively. Complex **1** exhibits a blue emission with a CIE coordinate of (0.1926, 0.148). The fluorescence emission spectra of the ligands are mainly attributed to $\pi^* \rightarrow n$ or $\pi^* \rightarrow \pi$ electronic transition.[34,35] Based on

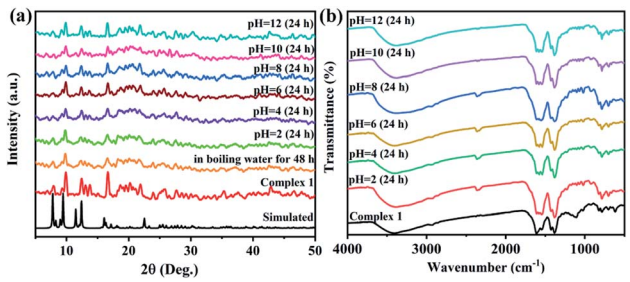


Fig. 3 (a) PXRD spectra of complex **1** under boiling water and in the solutions with different pH values. (b) IR spectra of complex **1** under different pH values.

the $d^{10}$ electronic configuration of Cd(II) ion, the fluorescence spectra of **1** may be attributed to the intraligand electron transfer, but not the charge transfer between metal ions and ligands.[36] The quantum yield of solid-state **1a** is about 2.24%, and the fluorescence lifetime is 3.749 μs (Fig. S4 and Table S4†). Moreover, the liquid-state emission spectra of **1** in different solvents are shown in Fig. S3,† including $H_2O$, acetone, $CH_2Cl_2$, DMA, DMF, DMSO, EtOH, $CHCl_3$, MeOH, $CH_3CN$. The emission intensity of **1** is strongly dependent on the organic solvent, and **1** scattered in MeOH exhibits the strongest emission intensity.

As mentioned above, complex **1** possesses an anionic framework and cellular channels, which can be used to encapsulate lanthanide ions for tunable luminescence. The sample of **1** was immersed in the aqueous solutions with Ln(III) (Ln = Eu or Tb) to obtain the Ln(III)@**1** materials with the Ln(III) in the channels. With increasing the soaking time of complex **1** in aqueous solutions with Eu(III) or Tb(III), the characteristic peak of Eu(III) or Tb(III) in Ln(III)@**1** increased with different CIE coordinates (Fig. 4 and Table S3†). When the sample of **1** was immersed in aqueous solution with Eu(III) ions for 2 h, 4 h, 8 h, 12 h, 14 h, 24 h and 48 h, the fluorescence emission spectrum of **1a** contains the characteristic peaks of **1** and Eu(III) ion, located at 463 nm, 598 nm, 623 nm, and 702 nm, respectively. At 48 h, the characteristic emission intensity of Eu(III) is the maximum, which appear as red emission with CIE coordination at (0.2943, 0.2499). The ICP data indicate that the doped amount of Eu(III) ion is about 10.8% corresponding to 1.09Eu(III)@**1** (**1a**) (Table S3†). The quantum yield of **1a** is about 5.76%, and the fluorescence lifetime is 3.588 μs (Fig. S4 and Table S4†).

Similarly, Tb(III) ions can also be introduced to the channels of **1** at room temperature. For Tb@**1**, the fluorescence emission spectra contain the characteristic peaks of **1** and Tb, located at 463 nm, 495 nm, 551 nm, 590 nm, and 627 nm, respectively. At 48 h, the emission intensity of Tb@**1** at 551 nm is the maximum with green emission, where the CIE coordination is at (0.3788, 0.532). Its doped amount of Tb(III) ion is about 6.81% to obtain 0.658Tb(III)@**1** (**1b**). The quantum yield of **1b** is about 13.6% with the fluorescence lifetime of 3.482 μs. The relative molar ratios of Eu(III), Tb(III), and Cd(III) in these MOFs were calculated by inductively coupled plasma (ICP) (Table S3†). In addition, the fluorescence properties of **1b** suspension at different pH were tested at room temperature (Fig. S5†). At pH = 1, the framework of **1** was destroyed, and the fluorescence emission spectrum of **1b** only contains the characteristic peak of **1** at 463 nm. At pH = 2–7, the framework of **1** has on changed (Fig. 3a), and the fluorescence emission spectrum of **1b** contains the characteristic peaks of **1** and Tb(III), where the emission intensity of **1b** at pH = 7 is the strongest.

Additionally, considering the strongest blue emission of **1** in MeOH, the emission of the Ln(III)@**1** solution can be fine tuned to be a white-light-emission by changing the molar ratio of Eu(III) and Tb(III) due to the red emission of Eu(III) and the green emission of Tb(III). The titration experiments of Eu(III) and Tb(III) in the suspended solution of **1** show that the characteristic emissions of Eu(III) and Tb(III) ions change from 5 : 0 to 5 : 60 (Fig. 5a). Their CIE coordinations exhibit that a white-light emission suspension is obtained with a CIE coordination of (0.3011, 0.3265) by addition of Eu(III) and Tb(III) molar ratio of 5 : 60 (Fig. 5b and Table S5†). Fig. 5c displays that the color variation from **1** to Ln(III)@**1** exhibits an obvious change between blue, red, orange, yellow and white with increasing the Eu : Tb molar ratio.

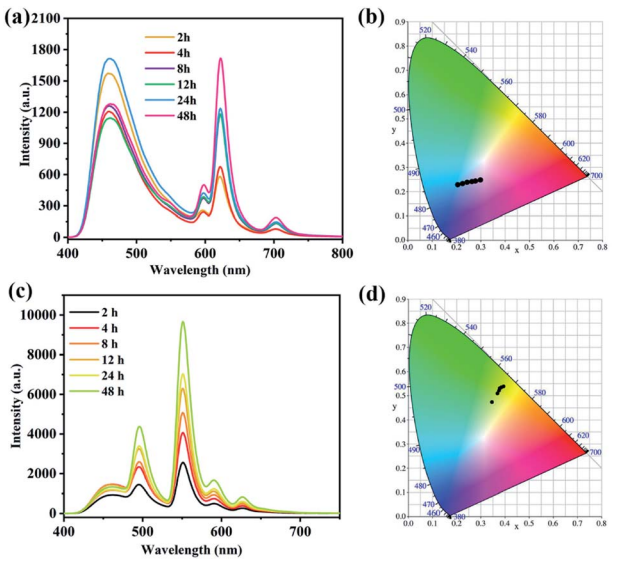


Fig. 4 (a) Fluorescence emission spectra of complex **1** immersed in aqueous solution with Eu(III) ions for different time. (b) The corresponding CIE coordinates for fluorescence emission spectra of Eu(III)@**1**. (c) Fluorescence emission spectra of complex **1** immersed in aqueous solution with Tb(III) ions for different time. (d) The corresponding CIE coordinates for fluorescence emission spectra of Tb(III)@**1**.

### 3.4. Selective sensing of bilirubin in PBS and human serum

Bilirubin is an important basis for clinical judgment of jaundice and a crucial index of liver function.[37] The above-mentioned

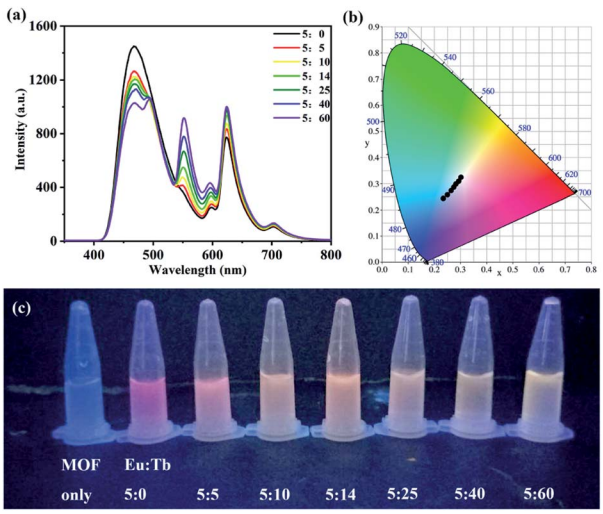


Fig. 5 The emission spectra of **1** in MeOH with Ln(III) ions at $\lambda_{ex}$ = 325 nm (a), the corresponding CIE coordinates (b) and the emission color changes under UV light at 254 nm (c) with varying the Eu : Tb molar ratio (5 : 0 to 5 : 60).

performance of **1b** encouraged us to further explore the fluorescent sensing for bilirubin. The emission spectra of **1b** scattered in 2 mL phosphate buffer solution (PBS, pH = 7.4) with various analytes that may consist in serum sample were recorded, including $Al^{3+}$, $Ag^{+}$, $Ca^{2+}$, $Cu^{2+}$, $K^{+}$, $Mg^{2+}$, $Na^{+}$, $Zn^{2+}$, $CO_3^{2-}$, $HCO_3^{-}$, $HPO_4^{2-}$, $NO_3^{-}$, uric acid (UA), ascorbic acid (AA), glycine (Gly), methionine (Met), phenylalanine (Phe), cysteine (Cys), bilirubin (BR). As shown in Fig. 6a, the luminescence intensity of **1b** at 552.4 nm is almost completely quenched with adding bilirubin, but the others have no obvious effect on the emission intensity of **1b**, which indicates that **1b** can effectively identify BR in the PBS. Selectivity is a crucial factor to determine whether **1b** can be applied as a sensor in practice. Some common metal ions and amino acids were selected for anti-interference experiment to judge the selectivity of **1b** for BR. Fig. 6b shows that the quenching efficiency of **1b** is almost unchanged within anti-interference substances, indicated that **1b** has good selectivity. The fluorescence "turn-off" induced by bilirubin were researched to estimate whether the developed fluorescent probe can be used for quantitative detection of bilirubin. As shown in Fig. 6c, when the concentration of BR was gradually increasing, the fluorescence intensity at 552.4 nm of **1b** gradually decreased, and when the BR concentration reached 1.25 mmol, the quenching rate of **1b** reached 96.2%, which suggests that **1b** can identify BR quantitatively and efficiently. In addition, the concentration of BR and the fluorescence intensity of **1b** have a good liner relationship (Fig. 6d), which conforms to the Stern–Volmer equation: $I_0/I = [BR] \times K_{sv} + 1$. $K_{sv}$ is the Stern–Volmer constant, $I_0$ and $I$ are the luminescence intensities without and with the addition of BR, respectively. By the calculation, $K_{sv}$ is about $3.6 \times 10^4$ $M^{-1}$ and the low limit detection (LOD) is about 0.250 μM.[38] The LOD was obtained by corresponding equation $3\delta/K_{sv}$, where $\delta$ is the blank standard deviation measurement (Fig. S6†). Compared with the reported MOFs for bilirubin recognition, **1b** exhibits relatively high sensitivity, which can be expected to be applied in real samples (Table S6†). The LOD is much less than the reported safety BR content (<17.1 μM) in the human serum.[39] Moreover, reproducibility is another important index to evaluate the actual use of **1b**. The fluorescence intensity has hardly changed after repeated for five times (Fig. S7a†), which lays an important foundation for the practical use of **1b**. In addition, time-dependent experiment was conducted (Fig. S7b†). The florescence intensity of **1b** was quenched rapidly within 30 s after addition of BR, and the florescence intensity remained unchanged within 6 minutes. The results indicate that **1b** exhibits effective and sensitive detection for BR in PBS.

To further prove the feasibility of the fluorescent probe, we try to carry out **1b** as a sensor to detect BR in serum (Fig. S8†). At the BR concentration of 2.5 mM, the quenching efficiency can reach 97.5%. The calculated $K_{sv}$ value is $3.23 \times 10^4$ and the LOD value is 0.279 μM. The recoverability of BR was tested in human serum sample. The recovery rate of BR is 99.20–101.9% and relative standard deviation (RSD) is 2.8–3.8% that is less than 5% (Table 2). It shows that the material has high accuracy for detection of BR in human serum. In addition, the sensing and detection ability of **1** towards BR has also been investigated in phosphate buffer solution (Fig. S9†). The calculated $K_{sv}$ value is $8 \times 10^3$ $M^{-1}$ and the LOD value is 1.125 μM that is higher than that for **1b**. The result indicates that **1b** exhibits the stronger detection ability for bilirubin.

Furthermore, the sensing mechanism of **1b** toward BR was explored in detail. The fluorescence lifetimes of **1b** and **1b-BR** are 3.482 μs and 3.371 μs, which exhibit that the quenching of **1b** by BR is mainly static quenching (Table S4†).[40–44] According to the PXRD spectrum, the skeleton of **1b** remains intact after the reaction with BR, which indicates that the fluorescence quenching is not because of the collapse of the structure (Fig. S10a†). The energy transfer process may cause the fluorescence quenching, which can be verified by recording the emission spectrum of the MOF and the UV-vis absorption of BR.[45] Compared with other substances (the UV absorption peaks of other metal ions and amino acids distribute in the range of 200–300 nm), the UV absorption pattern of BR has a large overlap with the fluorescence emission spectrum of **1b** in 430–610 nm, indicating that resonance energy transfer (RET) is an important reason for fluorescence quenching (Fig. S11a†). In addition, the XPS test was carried out, and the results proved that the peaks of Tb 4d and O 1s changed after the **1b** was soaked in BR solution (Fig. S11b†). The O 1s peak value of **1b** changes from 531.51 eV to 531.77 eV after detecting BR (Fig. S11c†), and the peak value of Tb 4d changes from 150.79 eV

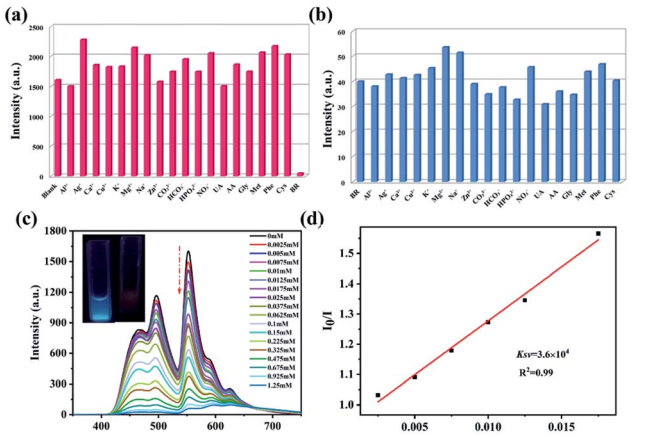


Fig. 6 (a) Fluorescence intensity of **1b** dispersed in various metal ion solutions and amino acid solutions at 552.4 nm. (b) Competitive quenching experiment of **1b** for the selective recognition of BR. (c) Fluorescence spectra of **1b** with addition of BR. (d) SV plot of **1b** for sensing of BR in phosphate buffer solution.

Table 2 The recovery test of bilirubin in human serum samples with different concentration

| Sample | Added BR (μM) | Found (μM) | Recovery (%) | RSD (%, $n = 3$) |
|---|---|---|---|---|
| Human serum | 0 | 1.900 | — | 3.0 |
| | 5 | 6.680 | 95.60 | 2.8 |
| | 10 | 11.82 | 99.20 | 3.3 |
| | 15 | 17.19 | 101.9 | 3.6 |

to 168.6 eV (Fig. S11d†). It shows that the O atoms and Tb(III) ions in **1b** have weak interaction with BR, which may lead to fluorescence quenching. The infrared spectra further illustrate that there is a weak interaction between **1b** and BR (Fig. S10b†). Compared with the IR spectrum of the **1b**, the **1b** soaked in BR has a new absorption peak at 1155.2 $cm^{-1}$, which further shows the weak interaction between **1b** and bilirubin.

## 4. Conclusions

In summary, we have successfully obtained a novel Cd(II)-based MOF (**1**) with 2D honeycomb structures and 1D chain structures. Complex **1** exhibits high water stability and pH stability. The luminescence emission intensity of **1** is strongly dependent on the organic solvent, and **1** scattered in MeOH exhibits the strongest emission intensity. Considering the anionic framework and cellular channels of **1**, Ln(III)@**1** with multicolor luminescence property was constructed by post-synthetic modification process. 1.09Eu(III)@**1** (**1a**) and 0.658Tb(III)@**1** (**1b**) were obtained by soaking complex **1** in $Eu(NO_3)_3 \cdot 6H_2O$ and $Tb(NO_3)_3 \cdot 6H_2O$ aqueous solutions for 48 h, respectively. The liquid-state emission spectra of Ln(III)@**1** can be tuned by changing the Eu(III)/Tb(III) molar ratio in solution, and the color variation from **1** to Ln(III)@**1** exhibits an obvious change between blue, red, orange, yellow and white with increasing the Eu(III) : Tb(III) molar ratio. A white-light emission suspension is obtained with a CIE coordination of (0.3011, 0.3265) by addition of Eu(III) and Tb(III) molar ratio of 5 : 60. Furthermore, **1b** can be developed into a fluorescent "turn-off" probe for detecting BR with high antijamming, excellent selectivity (LOD = 0.250 μM), and good recyclability in phosphate buffer solution (pH = 7.4). The fluorescent probe also can be applied to detect BR in serum with a LOD of 0.279 μM. The possible fluorescent "turn-off" mechanisms were studied in detail by PXRD, UV-vis spectroscopy and XPS. The post-synthetic modification process is a useful way to prepare Ln-MOF with multicolor luminescence property, which is significance for the development Ln-MOF fluorescent probe.

## Conflicts of interest

There are no conflicts to declare.

## Acknowledgements

The authors gratefully acknowledge the financial support of this work by the Natural Science Foundation of China (Grant No. 21601163, 22078309), Program for the Top Young Academic Leaders of North University of China (QX201906), Scientific and Technologial Innovation Programs of Higher Education Institutions in Shanxi (2019L0579) and Research Fund for the Doctoral Program of Liaocheng University (Grant No. 318051512).

## References

1 J. Fevery, *Liver Int.*, 2008, **28**, 592–605.
2 S. K. Chou and M. J. Syu, *Biomaterials*, 2009, **30**, 1255–1262.
3 J. J. Niu, G. J. Cheng and S. J. Dong, *Chin. J. Chem.*, 1994, **12**(1), 1–10.
4 Y. R. Du, X. Q. Li, X. J. Lv and Q. Jia, *ACS Appl. Mater. Interfaces*, 2017, **9**, 30925–30932.
5 C. J. Zhang, W. B. Bai and Z. P. Yang, *Electrochim. Acta*, 2016, **187**, 451–456.
6 J. G. Bell, M. P. S. Mousavi, M. K. Abd El-Rahmana, E. K. W. Tan, S. Homer-Vanniasinkam and G. M. Whitesides, *Biosens. Bioelectron.*, 2019, **126**, 115–121.
7 B. T. Doumas, B. W. Perry, E. A. Sasse and J. V. J. Straumfjord, *Clin. Chem.*, 1973, **19**, 984–993.
8 U. Behnke, *Food/Nahrung*, 1984, **28**, 676.
9 C. Wang, G. F. Wang and B. Fang, *Microchim. Acta*, 2009, **164**, 113–118.
10 R. R. Anjana, J. S. J. S. Anjali Devi, M. Jayasree, R. S. Aparna, B. Aswathy, G. L. Praveen, G. M. Lekha and G. Sony, *Microchim. Acta*, 2018, **185**, 1–11.
11 Y.-Y. Yuan, S.-L. Yang, C.-X. Zhang and Q.-L. Wang, *CrystEngComm*, 2018, **20**, 6989–6994.
12 P. P. Sun, Z. Wang, Y. T. Bi, D. Sun, T. Zhao, F. F. Zhao, W. S. Wang and X. Xin, *ACS Appl. Nano Mater.*, 2020, **3**, 2038–2046.
13 Z. Chen, Y. W. Sun, L. L. Zhang, D. Sun, F. L. Liu, Q. G. Meng, R. M. Wang and D. F. Sun, *Chem. Commun.*, 2013, **49**, 11557–11559.
14 L. L. Zhang, Z. X. Kang, X. L. Xin and D. F. Sun, *CrystEngComm*, 2016, **18**, 193–206.
15 W. M. Chen, X. L. Meng, G. Zhuang, Z. Wang, M. Kurmoo, Q. Zhao, X. Wang, B. Shan, C. Tung and D. Sun, *J. Mater. Chem. A*, 2017, **5**, 13079–13085.
16 Y. Rachuri, B. Parmar and E. Suresh, *Cryst. Growth Des.*, 2018, **18**, 3062–3072.
17 B. Parmar, Y. Rachuri, K. K. Bisht, R. Laiya and E. Suresh, *Inorg. Chem.*, 2017, **56**, 2627–2638.
18 B. Parmar, K. K. Bisht, Y. Rachuri and E. Suresh, *Inorg. Chem. Front.*, 2020, **7**, 1082–1107.
19 *Metal Organic Frameworks*, ed. V. Mittal, Central West Publishing, Australia, 2019, pp. 187–238.
20 Z. H. Yan, L. L. Han, Y. Q. Zhao, X. Y. Li, X. P. Wang, L. Wang and D. Sun, *CrystEngComm*, 2014, **16**, 8747–8755.
21 S. Yuan, Y. K. Deng and D. Sun, *Chem.–Eur. J.*, 2014, **20**, 10093–10098.
22 L. Yang, Y. Dou, L. Qin, L. L. Chen, M. Z. Xu, C. Kong, D. P. Zhang, Z. Zhou and S. Wang, *Inorg. Chem.*, 2020, **59**, 16644–16653.
23 J. Tang, D. D. Feng, J. Yang, X. H. Ma and X. Q. Wang, *New J. Chem.*, 2020, **44**, 8728–8735.
24 M. H. Dehghani, M. M. Taher, A. K. Bajpai, B. Heibati, I. Tyagi, M. Asif, S. Agarwal and V. K. Gupta, *Chem. Eng. J.*, 2015, **279**, 344–352.
25 X. Y. Zhu, B. Li, J. Yang, Y. S. Li, W. R. Zhao, J. L. Shi and J. L. Gu, *ACS Appl. Mater. Interfaces*, 2015, **7**, 223–231.
26 X. Q. Wang, X. H. Ma, D. D. Feng, J. Tang, D. Wu, J. Yang and J. J. Jiao, *Cryst. Growth Des.*, 2021, **21**, 2889–2897.
27 X. D. Zhu, K. Zhang, Y. Wang, W. W. Long, R. J. Sa, T. F. Liu and J. Lu, *Inorg. Chem.*, 2018, **57**, 1060–1065.

28 D. C. Ma, G. Han, Z. F. Gao and S. B. Chen, *ACS Appl. Mater. Interfaces*, 2019, **11**, 45290–45300.
29 X. Q. Wang, D. D. Feng, Y. D. Zhao, D. D. Fang, J. Tang, L. M. Fan and J. Yang, *J. Solid State Chem.*, 2019, **274**, 40–46.
30 X. P. Wang, L. L. Han, Z. Wang, L. Y. Guo and D. Sun, *J. Mol. Struct.*, 2016, **1107**, 1–6.
31 D. Sun, L. L. Han, S. Yuan, Y. K. Deng, M. Z. Xu and D. F. Sun, *Cryst. Growth Des.*, 2013, **13**, 377–385.
32 A. L. Speck, *PLATON. a multipurpose crystallographic tool*, Utrecht University, Utrecht, The Netherlands, 2001.
33 A. L. Speck, Multipurpose crystallographic tool, *J. Appl. Crystallogr.*, 2003, **36**, 7–13.
34 L. F. Xu, Y. Xu, X. L. Li, Z. P. Wang, T. Sun and X. Zhang, *Dalton Trans.*, 2018, **47**, 16696–16703.
35 Z. W. Zhai, S. H. Yang, M. Cao, L. K. Li, C. X. Du and S. Q. Zang, *Cryst. Growth Des.*, 2018, **18**, 7173–7182.
36 L. M. Fan, Y. J. Zhang, J. F. Liang, X. Q. Wang, H. X. Lv, J. Wang, L. Zhao and X. T. Zhang, *CrystEngComm*, 2018, **20**, 4752–4762.
37 I. Taurino, V. Van Hoof, G. De Micheli and S. Carrara, *Thin Solid Films*, 2013, **548**, 546–550.
38 P. Kannan, H. Chen, V. T. Lee and D. Kim, *Talanta*, 2011, **86**, 400–407.
39 C. Xia, Y. Xu, M. M. Cao, Y. P. Liu, J. F. Xia, D. Y. Jiang, G. H. Zhou, R. J. Xie, D. F. Zhang and H. L. Li, *Talanta*, 2020, **212**, 120795.
40 D. D. Feng, Y. D. Zhao, X. Q. Wang, D. D. Fang, J. Tang, L. M. Fan and J. Yang, *Dalton Trans.*, 2019, **48**, 10892–10900.
41 R. Dalapati, U. Kokcam-Demir, C. Janiak and S. Biswas, *Dalton Trans.*, 2018, **47**, 1159–1170.
42 Y. Rachuri, B. Parmar, K. K. Bisht and E. Suresh, *Dalton Trans.*, 2016, **45**, 7881–7892.
43 H. Liu, J. Rong, G. Shen, Y. Song, W. Gu and X. Liu, *Dalton Trans.*, 2019, **48**, 4168–4175.
44 C. Gogoi, M. Yousufuddin and S. Biswas, *Dalton Trans.*, 2019, **48**, 1766–1773.
45 X. Q. Wang, D. D. Feng, J. Tang, Y. D. Zhao, J. Li, J. Yang, C. K. Kim and F. Su, *Dalton Trans.*, 2019, **48**, 16776–16785.